Orbital-selective chemical functionalization of MoS_2 by Fe

Niels Ehlen,[1,*] Yannic Falke,[1,†] Boris V. Senkovskiy,[1] Timo Knispel,[1] Jeison Fischer,[1] Oliver N. Gallego,[1] Cesare Tresca,[2] Maximilian Buchta,[1] Konstantin P. Shchukin,[1,3] Alessandro D'Elia,[1] Giovanni Di Santo,[4] Luca Petaccia,[4] Dmitry Smirnov,[5] Anna Makarova,[6] Gianni Profeta,[7] Thomas Michely,[1] and Alexander Grüneis[1,3,‡]

[1]*II. Physikalisches Institut, Universität zu Köln, Zülpicher Strasse 77, 50937 Köln, Germany*

[2]*CNR-SPIN, Università degli studi dell'Aquila, Via Vetoio 10, I-67100 L'Aquila, Italy*

[3]*Institut für Festkörperelektronik, Technische Universität Wien, Gußhausstraße 25, 1040 Vienna, Austria*

[4]*Elettra Sincrotrone Trieste, Strada Statale 14 km 163.5, 34149 Trieste, Italy*

[5]*Institute of Solid State and Materials Physics, Technische Universität Dresden, 01062 Dresden, Germany*

[6]*Physikalische Chemie, Institut für Chemie und Biochemie, Freie Universität Berlin, Arnimallee 22, 14195 Berlin, Germany*

[7]*Dipartimento di Scienze Fisiche e Chimiche CNR-SPIN, Università degli Studi dell'Aquila, Via Vetoio 10, I-67100 L'Aquila, Italy*

(Received 26 October 2022; revised 6 October 2023; accepted 8 November 2023; published 22 November 2023)

The occupied electron energy bands of monolayer MoS_2 are composed from out-of-plane d orbitals at the Brillouin zone (BZ) center and from in-plane d orbitals at the BZ corner. If a dopant would interact in an orbital selective manner with the MoS_2 bands, it could provide a tuning knob to modulate the MoS_2 energy bands according to the electron wave vector. Here we directly show by angle-resolved photoemission spectroscopy (ARPES) that Fe doping of epitaxial MoS_2 is orbital selective. That is, Fe doping causes a larger energy upshift of the valence band at the BZ center compared to the BZ corner. The optical properties of Fe-doped MoS_2 are investigated by ultrahigh vacuum photoluminescence and reveal a loss of photoluminescence upon Fe doping. The sample morphology is investigated by scanning tunneling microscopy and shows a two-dimensional core-shell structure with Fe chemisorbed along the edge of MoS_2 islands. This structural determination is consistent with core-level spectroscopy measurements. Realistic *ab initio* calculations and tight-binding calculations of the electronic band structure fully explain ARPES and photoluminescence experiments and highlight that dopants with complex d-orbital structure interact with MoS_2 in an orbital-sensitive manner. Our approach opens opportunities in band-structure engineering of two-dimensional materials.

DOI: 10.1103/PhysRevB.108.195430

I. INTRODUCTION

In a 1H-MoS_2 monolayer which has a trigonal prismatic symmetry (D_{3h} point group), crystal-field splitting results in three distinct Mo energy levels with d character: the lowest level with d_{z^2} orbital character; a degenerate level of $d_{xy}, d_{x^2-y^2}$ orbitals; and the highest level composed out of the degenerate d_{xz}, d_{yz} orbitals [1,2]. When forming energy bands in the 1H-MoS_2 solid, the orbitals mix and four out of the six Mo electrons are transferred to the S atoms. The remaining two electrons completely fill the valence band (VB) with partial d_{z^2}, d_{xy}, and $d_{x^2-y^2}$ orbital character [3]. As a consequence, the chemical potential lies above the lowest band with d character and four out of the five bands with d orbital character are empty [3]. The multiorbital nature of the VB wave function is evident in different regions of the Brillouin zone (BZ) where the wave function has a distinct character. That is, the VB maxima which are located at Γ and K points have out-of-plane d_{z^2} and in-plane d_{xy}, $d_{x^2-y^2}$ character, respectively. In a tight-binding (TB) picture, the d orbital energies are encoded in the on-site energies (diagonal terms) of the TB Hamiltonian [3]. The on-site term for the d_{z^2} orbitals has a different value from the on-site terms for the $d_{x^2-y^2}$ and d_{xy} orbitals which are equal to each other [3]. The modification of these on-site terms is key to controlling the energies of the VB maxima at Γ and K points, which play an important role for optical properties. A small modification of the d on-site energies can significantly change the band structure, e.g., from direct band gap to indirect band gap semiconductor. The band structure change has, by proxy, a large effect on the optical properties. For example, monolayer MoS_2 has a direct band gap while bilayer MoS_2 has an indirect band gap [4]. The multiorbital character of MoS_2 could, in principle, provide opportunities for band-structure engineering if one could selectively change the energy of only some of the d orbitals (i.e., to shift d_{z^2} and d_{xy}, $d_{x^2-y^2}$ energies differently). Strain engineering [5] is an option to modify the d-orbital energies in MoS_2. However, the engineering of homogeneous strain fields is difficult to achieve over large areas in MoS_2 grown by molecular beam epitaxy (MBE). This is why the adsorption of dopant atoms on the surface of a MoS_2 monolayer is a tempting route [6]. Experimentally, it was shown that alkali metal doping of bulk MoS_2 changes the size of the band gap but does not result in a change from indirect to direct semiconductor [7]. The absence of orbital selectivity can be understood by the nondirectional s

*ehlen@ph2.uni-koeln.de
†falke@ph2.uni-koeln.de
‡alexander.grueneis@tuwien.ac.at

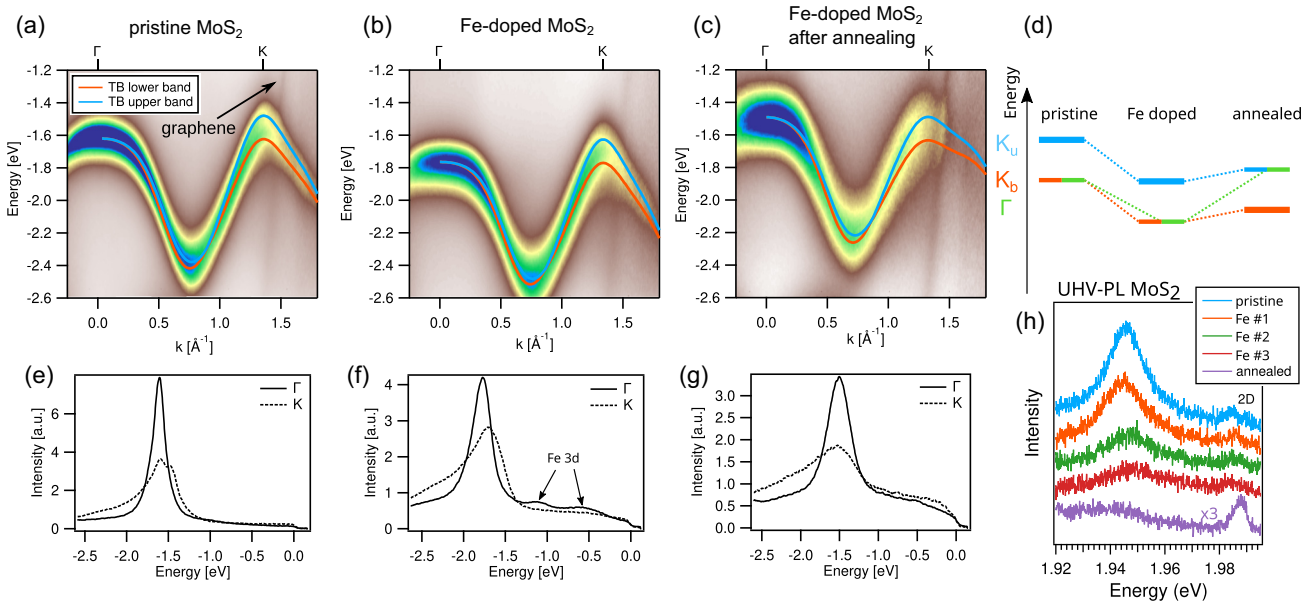

FIG. 1. ARPES ($h\nu = 32$ eV, $T = 15$ K) of (a) pristine MoS_2, (b) Fe-doped MoS_2 (0.05 Å Fe coverage), and (c) Fe-doped MoS_2 after annealing to RT. ARPES spectra have been recorded along the ΓK direction of the 2D BZ. The lines denote tight-binding (TB) calculations. (d) Schematics of the K point and Γ point energies. The labels K_u and K_b denote the energies of the upper and lower spin-orbit split bands at K point and the label Γ denotes the energy at Γ point. [(e)–(g)] Energy dispersion curves (EDCs) through the Γ and K points of MoS_2. These EDCs are obtained by cutting through the ARPES spectra shown in [(a)–(c)] at wave vectors Γ and K. The energy $E = 0$ in the EDCs corresponds to the Fermi level. (h) Ultrahigh vacuum photoluminescence (UHV-PL) as a function of Fe doping for three Fe doses in steps of 0.016 Å and after annealing to RT (all measurements at $T = 5$ K). The purple trace for the Fe-doped sample after annealing is multiplied by a factor of 3.

orbital character of the alkali metal and the ionic nature of the interaction. This poses the question if dopants with more complex orbitals are able to interact in an orbital selective manner. In the present paper, we show that Fe interacts in an orbital selective way with MoS_2, whereby MoS_2 is transformed from a direct band gap semiconductor into an indirect band gap semiconductor.

Previously, doping MoS_2 by transition metals (TMs) has been investigated theoretically in the context of inducing magnetism [8–11] or the valley Zeeman effect [12] in TMDCs. It has also been suggested that TM-doped MoS_2 is well suited to bind noble gases such as Xe and Kr [13]. A single TM atom in a freestanding TMDC can, in principle, be adsorbed on top of Mo_2 or form an interstitial or substitutional defect [10,11]. For a single Fe atom interacting with MoS_2, theory predicts that the formation energy for interstitial Fe is highest, followed by substitutional Fe and Fe adsorbed on top of Mo [11]. Other theoretical investigations agree that the most stable site for Fe adsorption is on top of Mo [13,14]. It has been shown by transmission electron microscopy that sulfur single and double vacancies in monolayer MoS_2 are rather common [15]. One important question in context of the present paper is under what circumstances these vacancies can be filled by Fe. The substitutional doping of a chalcogen vacancy by various TMs has been investigated theoretically for different TMDCs (MoS_2, $MoSe_2$, and $MoTe_2$) [11]. The filling of a chalcogen vacancy by a TM requires not only the energetic stability of the final state but also the overcoming of an energy barrier after TM adsorption. As a result of these calculations, the incorporation of Fe into sulfur vacancies of MoS_2 was found to be not energetically favorable for an isolated island and hence Fe is expected to stay on top of MoS_2 or at the edge of MoS_2. Nevertheless, it is not clear how this situation changes if MoS_2 is on a substrate and if the substitution close to the edge of an MoS_2 island can occur.

There are no studies on the effect of Fe doping on the electronic energy band structure and optical properties and the roles of temperature on the Fe-MoS_2 interaction have not been investigated. MoS_2 monolayers grown by MBE typically have small crystallite sizes for low coverage and therefore the edges of MoS_2 crystallites are important for their physical and chemical properties [16]. Yet, the interaction of TMs with the edges of epitaxial MoS_2 has not been studied. The present paper addresses these issues and investigates the electronic and optical properties as well as the sample morphology of Fe-doped epitaxial MoS_2/graphene and the effect of temperature.

II. RESULTS

A. Electronic band structure

Monolayer MoS_2 samples are grown on top of graphene by MBE according to a previous recipe [16]. These samples have monolayer thickness MoS_2 as evidenced by ARPES, photoluminescence (PL), and scanning tunneling microscopy (STM) measurements (see Methods). Figures 1(a)–1(c) show ARPES of pristine and Fe-doped MoS_2 as well as the Fe-doped MoS_2 after annealing to room temperature (see the Methods sections for experimental details). The ARPES data feature the intense MoS_2 band with two valleys around Γ and K points and a linear graphene band with a weak ARPES intensity. In the case of pristine and Fe-doped MoS_2 (before annealing), the VB maximum is located at K. After warming

TABLE I. Changes in tight-binding (TB) parameters for the on-site energies of Fe-doped MoS_2 and Fe-doped MoS_2 after annealing to room temperature. These values have been used in the calculation shown in Figs. 1(a)–1(c) and are responsible for the observed band structure changes at Γ and K points.

Change in on-site energy	Fe-doped MoS_2	Fe-doped MoS_2 after annealing
$\Delta\epsilon_{dz^2}$	−190 meV	340 meV
$\Delta\epsilon_{dx^2-y^2} = \Delta\epsilon_{dxy}$	−190 meV	280 meV

up the Fe-doped MoS_2/graphene sample to room temperature and cooling down again, we observe that the VB has approximately equal energy at Γ and K points. The sketch in Fig. 1(d) denotes VB maxima at K and Γ points and how their energies change as a function of Fe doping and annealing. In Figs. 1(e)–1(g), the energy dispersion curves (EDCs) through the Γ and K points for pristine, Fe-doped MoS_2 and Fe-doped MoS_2 after annealing are shown. The EDCs are obtained by cutting the 2D ARPES intensity of Figs. 1(a)–1(c) at the Γ and K points. This process of cutting the 2D ARPES intensity yields a one-dimensional graph of ARPES intensity versus binding energy (BE) for each wave vector. In the EDCs, features at energies $E \sim -0.5$ eV and $E \sim -1$ eV appear after Fe deposition. We assign these features to the Fe 3d levels. This assignment is in agreement to previous photoemission measurements of thin Fe films grown on Cu [17]. Finally, we note that the VBs of Fe-doped MoS_2 after annealing [Fig. 1(c)] are upshifted with respect to the pristine MoS_2 [Fig. 1(a)].

We now proceed to the interpretation of ARPES band structures via TB simulations of the energy band structure using a Hamiltonian, which employs d_{z^2}, d_{xy}, and $d_{x^2-y^2}$ orbitals and includes the spin-orbit coupling in the VBs [3,18]. The Fe atoms are not included in the TB calculations. We effectively model the adsorption of an Fe atom to MoS_2 by change of the on-site energies due to the interaction with Fe. Our calculations are performed as follows. We first fit all TB parameters to the ARPES data of pristine MoS_2. For simulations of Fe-doped MoS_2 and annealed Fe-doped MoS_2, we keep all parameters except the three on-site matrix elements for the d orbitals fixed within a 5% range. The changes of the on-site energies ϵ_{dz^2}, $\epsilon_{dx^2-y^2}$, and ϵ_{dxy} upon Fe doping and annealing are given in Table I. We are able to fully reproduce the observed ARPES data of Fe-doped MoS_2 and Fe-doped MoS_2 after annealing. The change in ϵ_{dz^2} is larger than that of $\epsilon_{dxy} = \epsilon_{dx^2-y^2}$ parameters. This indicates that the out-of-plane orbitals are affected more by the Fe dopants than the in-plane orbitals. The ARPES data in Figs. 1(a)–1(c) are overlaid with the results of the TB calculation.

B. Optical properties

Sample synthesis, Fe doping, and PL measurements were carried out in ultrahigh vacuum (UHV) conditions (see Methods). The UHV-PL setup used in this paper has also been used in a previous experiment studying PL of alkali metal doped TMDC heterostructures [19]. For the pristine samples, we obtain sharp PL spectra at an energy of 1.946 eV with a FWHM of ∼15 meV as shown in Fig. 1(h). We performed Fe doping in three steps with the sample at 5 K during Fe deposition and PL measurement. In each Fe deposition, we used one-third of the total Fe amount compared to what we had deposited in the ARPES experiment. After each Fe deposition, we perform PL measurement. The Fe deposition results in small blueshifts (∼10 meV) of the PL peak position and a reduced PL intensity. We attribute the small shift to the concomitant changes of the quasiparticle band gaps and exciton BEs which cancel each other [20]. The lower PL intensity after Fe evaporation could be due to Fe atoms and clusters promoting radiationless decay of the optical excitation. After three cycles of Fe evaporation [dark red curve in Fig. 1(h)], the deposited amount of Fe is identical to that in ARPES. Upon warmup to room temperature and subsequent cooldown, we observe the disappearance of PL (the purple curve in Fig. 1(h) was multiplied by a factor of 3 with the graphene 2D mode as a reference and no PL is visible). The absence of PL can be understood by the change of direct to indirect band gap, which we assign to the shift of the VB maximum from the K to Γ point as observed by ARPES and the TB calculations.

C. Scanning tunneling microscopy

The changes observed in ARPES and PL upon warming MoS_2 with adsorbed Fe are likely caused by surface diffusion of Fe or a chemical reaction between Fe and MoS_2 that is activated by temperature. We perform STM to investigate the structure of Fe adsorbed to MoS_2/graphene. This is important for the construction of a realistic atomic model needed as input for *ab initio* calculations (see Sec. IV B). We have studied the adsorption process of Fe by STM using nearly the double amount of deposited Fe compared to ARPES and PL experiments, i.e., 0.08 Å, to be able to easily visualize Fe. Figures 2(a)–2(c) depict STM images for pristine MoS_2, Fe-doped MoS_2, and Fe-doped MoS_2 after annealing to room temperature, respectively. After Fe deposition, we observe small protrusions which are attributed to single Fe atoms and small Fe clusters [Fig. 2(b)]. The low deposition temperature of 30 K largely prevents diffusion and thereby suppresses formation of larger clusters. Our observations are consistent with the predominant presence of single Fe adatoms on MoS_2/Au(111) after deposition of a small amount of Fe at a temperature less than 10 K [21]. After annealing to room temperature, we observe that the small protrusions on graphene and on MoS_2 have disappeared, see Fig. 2(c). We also found that the morphology of the MoS_2 islands is changed, i.e., very few big clusters are found on top of MoS_2 islands. Most Fe is located at the edges of the MoS_2 islands forming a dense ring along the islands' circumferences. For better appreciation of the formed Fe rim, the Fe accumulation around the MoS_2 islands is highlighted in shaded blue in Fig. 2(c). Accumulation of Fe on the edge of the island is in line with the reported chemical activity of MoS_2 edges [22] and their use in catalysis. That is, Fe deposited onto MoS_2/graphene is

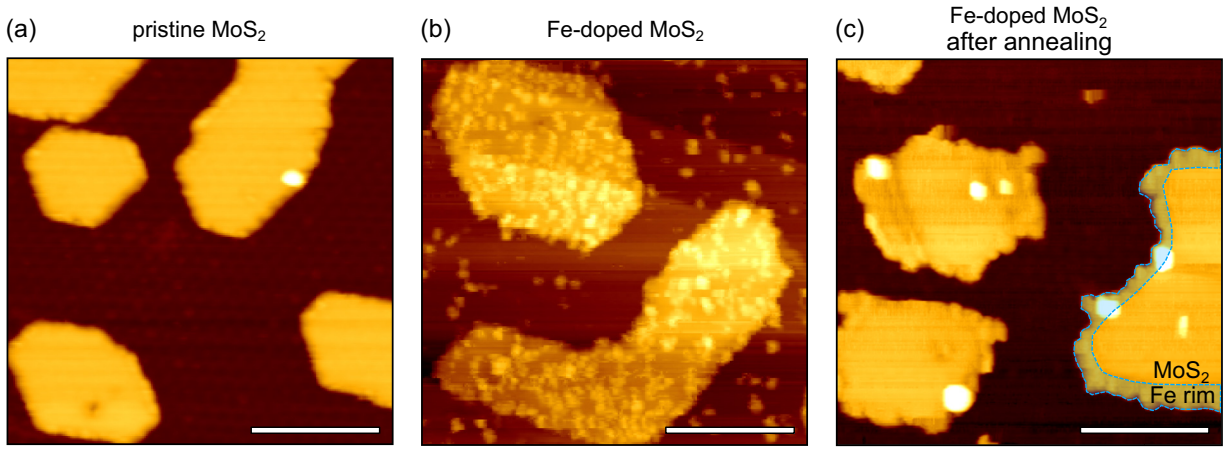

FIG. 2. Scanning tunneling microscopy (STM) characterization of 0.4 ML of MoS_2 grown on graphene/Ir(111) (a) before and (b) after deposition of Fe atoms at $T = 30$ K and (c) after annealing to room temperature. The Fe around the MoS_2 island edge is shaded in blue (Fe rim). Images in (a) and in (c) were recorded at room temperature and (b) was recorded at $T = 30$ K. STM image parameters: $V_b = 1.5$ V, $I_t = 0.1$ nA. The scale bar is 20 nm.

physisorbed and mobile at room temperature. Upon annealing, it chemically binds to the edges of MoS_2 islands forming a two-dimensional core-shell structure.

D. Core-level spectroscopy

We have performed x-ray photoelectron spectroscopy of the pristine and the Fe-doped sample after annealing for two different MoS_2 coverages corresponding to ∼0.5 ML and ∼0.3 ML. A larger (smaller) coverage results in larger (smaller) MoS_2 islands and, hereafter, these samples are labeled large islands and small islands, respectively. We performed XPS of MoS_2 core levels at the dipole beamline RGBL of the BESSY II electron storage ring operated by Helmholtz-Zentrum Berlin für Materialien und Energie. Figures 3(a) and 3(b) depict the spin-orbit split Mo 3*d* and S 2*p* core levels of small and large islands, respectively. We observe that the spin-orbit split core levels of Mo 3*d* have multiple components and our data are in good agreement to previous XPS data of MoS_2 islands on Au that was studied in the context of the catalytic activity of MoS_2 edges [23]. The Mo 3*d* line shape was modeled by three Doniach-Sunjic components at low BE, middle BE, and high BE [23] at fixed positions and widths. The colors used for these components are as follows: high BE (green), middle BE (blue), and low BE (orange) and are used in the fits in Fig. 3(a). This grouping into three chemical shifts as used in previous works [23] is supported by our *ab initio* calculations of the core-level shifts (see Methods section for details). Figure 3(c) gives a graphical summary of the calculated core-level shifts for Mo 3*d* depending on the environment of the Mo atom. The number close to the Mo atom position describes the calculated core-level shift. The model that we used to fit the Mo 3*d* core-level spectra of pristine and Fe-doped MoS_2 with a set of three BEs allows us to accurately reproduce all experimental XPS data. Note that the BEs of the three components are fixed to the calculated core-level shifts (see Sec. IV, Methods).

The high BE component (no core-level shift) of the Mo 3*d* core level is due to Mo atoms in the bulk of the MoS_2 island. The middle BE (0.3 eV–0.7 eV shift) is due to one of the following: Mo atoms close to the edge bound to three pairs of S atoms, Mo atoms having one of the three neighboring S pairs located on the edge, and Mo atoms next to a single or double S vacancy. The low BE component (0.7 eV–1 eV shift) is mostly due to Mo edge atoms that have only two pairs of S atoms as neighbors instead of three and in part to Mo atoms next to a S single/double vacancy. We believe that the pristine MoS_2 flakes have few sulfur vacancies compared to the number of edge atoms. Therefore, the main contribution to the middle and low BE components are not neighboring vacancies but Mo edge atoms. We observe that the MoS_2 sample with smaller islands has a larger component at middle and low BE than the MoS_2 sample with larger islands. This is due to the fact that the small MoS_2 islands have a larger surface-to-bulk ratio. Regarding the S 2*p* peak position, we observe a 200 meV higher BE for the small islands as compared to the large islands, which we attribute to unsaturated S atoms at the edge.

Let us now move to the Fe-doped MoS_2 flakes [lower panels of Figs. 3(a) and 3(b) and right part of Fig. 3(c)]. Upon Fe doping, we observe an increase of the low BE component (orange color). We attribute this increase to the presence of large Fe clusters at the edge as observed via STM [cf. Fig. 2(c)]. According to our calculations (Method section), the presence of Fe at the edge of the island reduces the Mo 3*d* core-level BE of Mo atoms close to Fe. The larger relative increase of the high Mo 3*d* core levels BE component for the small islands is due to their larger surface/bulk ratio compared to the large islands. The increase in the medium BE component is due to the presence of Fe atoms on the island edge. After Fe doping, the S 2*p* peaks for both island sizes move to the same energy of 161.9 eV for the S $2p_{3/2}$ peak. We attribute this to Fe atoms and clusters adsorbed to the islands' edges that saturate dangling S bonds.

E. *Ab initio* band structure of Fe-doped MoS_2

Next, we have investigated the electronic structure of MoS_2 upon Fe doping with a special focus on the location of the VB maximum. Figure 4 depicts DFT band-structure calculations

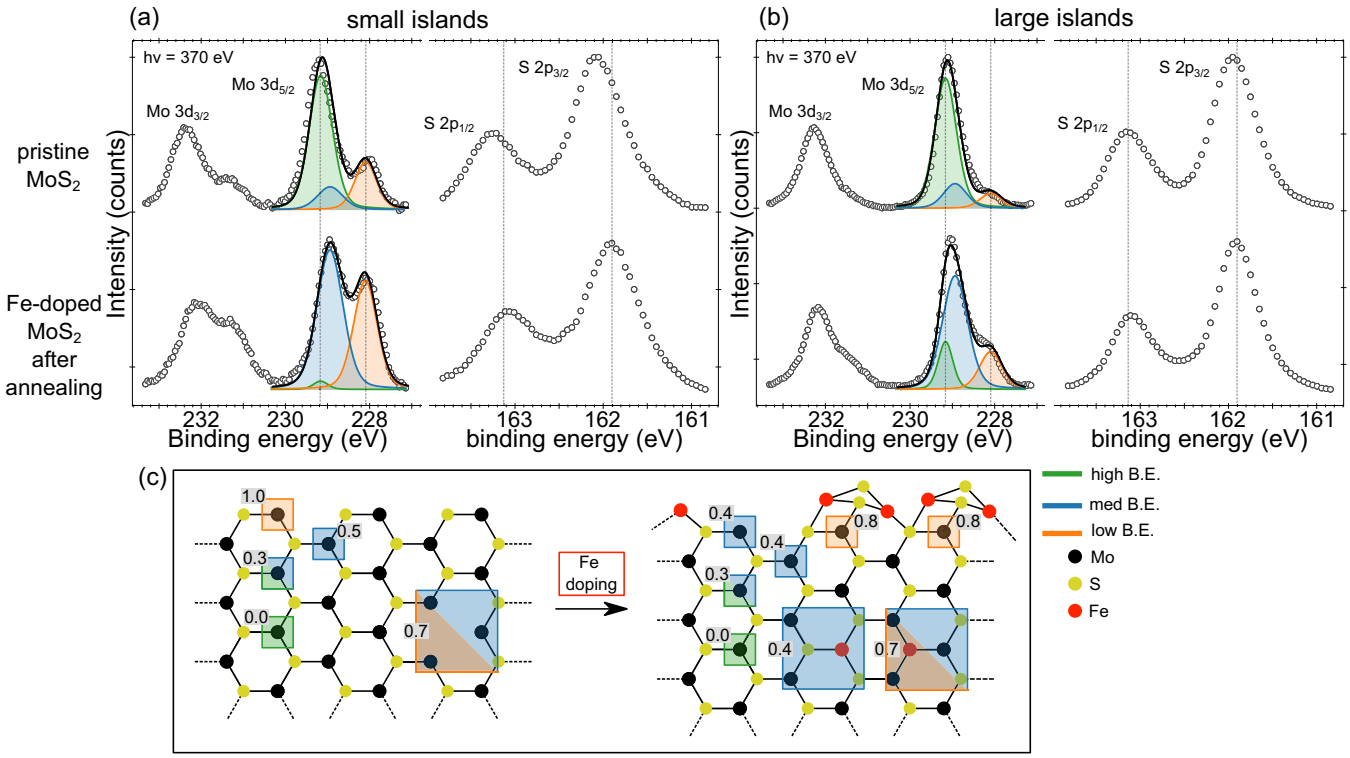

FIG. 3. X-ray photoemission spectroscopy (XPS) of Mo 3*d* and S 2*p* core levels of (a) small islands and (b) large islands before (upper row) and after (lower row) Fe deposition and annealing. The Doniach-Sunjic lineshape analysis of the Mo 3*d* core level is shown for the more intense spin-orbit split XPS line. The components at high binding energy (BE) in green, medium BE in blue, and low BE in orange denote the different Mo atom positions as shown in (c). The dashed vertical lines are guides to the eye and indicate the low and high BE components in Mo 3*d* and the S 2*p* position in the Fe-doped MoS_2. (c) Calculated relative shift of the Mo 3*d* core level BE with respect to the bulk component (green color) for the pristine (left) and Fe-doped MoS_2 (right). The Mo 3*d* core-level shift in pristine MoS_2 is a consequence of an Mo atom located at the edge or near a vacancy. Black, red, and yellow colored atoms denote Mo, Fe, and S, respectively.

of MoS_2 with Fe in various geometries. We have included the Fe sites that are considered energetically favorable (on top of MoS_2 and on the edge of MoS_2) and the unfavorable sites (substitutional Fe) for completeness. The calculations were performed without SOC included in a supercell geometry. The calculations we performed grasp the chemical-induced modification of the band structure and the SOC contribution does not alter the calculated energy shifts but induces a splitting of the bands which rigidly follows the band structure. The band structures were unfolded after calculation, projected on the corresponding *d* orbitals and compared to the band structure of pristine MoS_2. Figure 4(a) shows the energy band structure for Fe adsorbed on top of a MoS_2 layer. The unfolded band structure of Fe on top of MoS_2 has a VB maximum located at the *K* point. That is, there is no shift of the VB maximum for this geometry with respect to pristine MoS_2. Figure 4(b) is the band structure of defective MoS_2 with Fe replacing the S single vacancy site. Here, the VB maximum is shifted from the *K* point for the pristine layer to the Γ point. Figure 4(c) also depicts a defective MoS_2 band structure with a Mo vacancy filled by an Fe atom. In this case, the VB maximum is shifted to the zone center, too.

To understand the influence of Fe adsorbed to the edge of a MoS_2 island, we used the simplified model of Fe adsorbed at the edge of a MoS_2 armchair nanoribbon. Figure 4(d) depicts the top view and side view of a MoS_2 armchair nanoribbon with Fe atoms replacing Mo at its edge. The electronic structure of the nanoribbon can be understood by zone folding the band structure of a MoS_2 layer by cutting the 2D dispersion along so-called cutting lines that are parallel to the Γ*M* direction in the BZ. As a result, we obtain that both Γ and *K* points of the two-dimensional BZ are located on the one-dimensional $k = 0$ wave vector. The different effective masses of the VB at the Γ (larger) and *K* (smaller) points, allow us, together with the orbital character, to distinguish them when both are folded at the Γ point of the nanoribbon's BZ. To study the effect of Fe binding to the edge of MoS_2 in the electronic properties of the ribbon, we also project the calculated bands onto the atomic wave function centered on a Mo atom at the center and edge of the ribbon. Figure 4(e) reports the band structure projected onto a center atom: *K*-derived states are higher in energy with respect to Γ-derived states (blue), indicating that Fe decorating the edges of the ribbon does not perturb the *d* band dispersion in the interior of the ribbon. On the contrary, for the projection of the bands on Mo atoms at the edges of the ribbon, shown in Fig. 4(f), the energy ordering between *K* and Γ derived bands is inverted, indicating that Fe atoms that decorate the edges induce a local perturbation of the band structure. This is in agreement with the wave-function character of 2D MoS_2 and can also be seen in Figs. 4(b) and 4(c). Figure 4(g) depicts the set of cutting lines for the armchair ribbon used in the calculation indicating

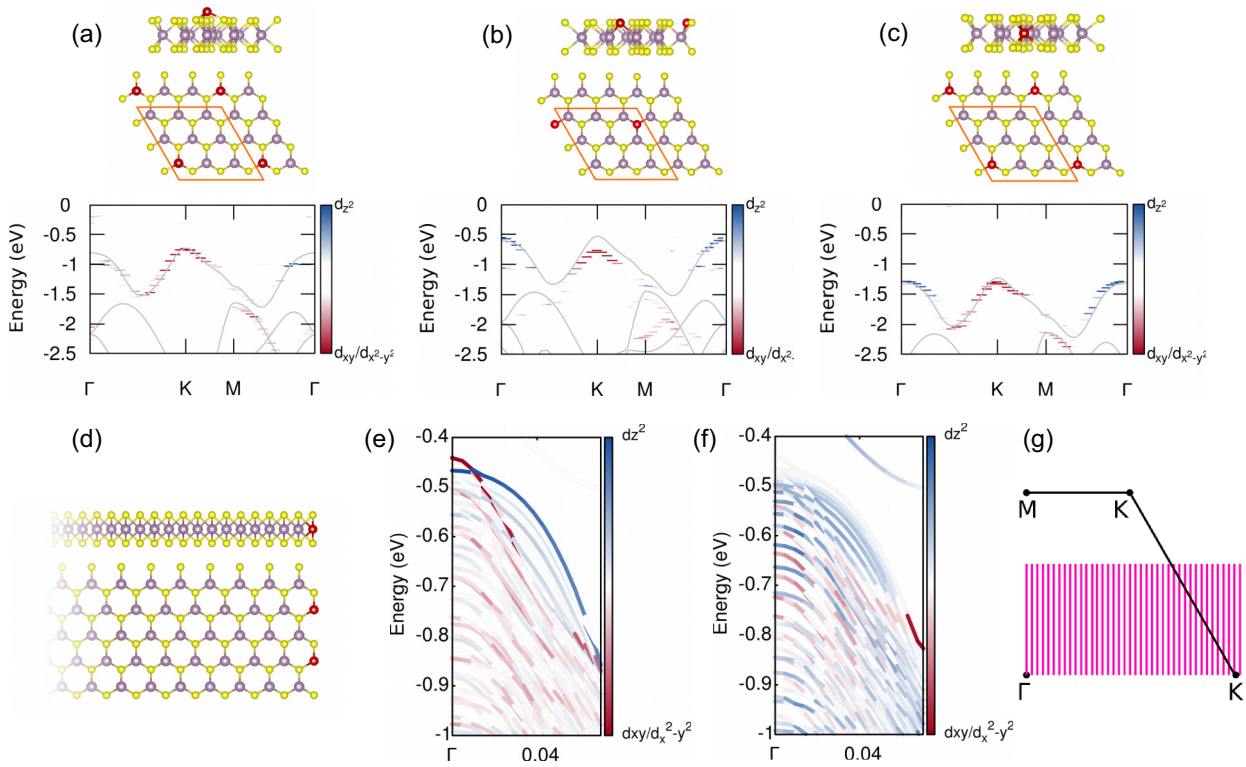

FIG. 4. (a) The crystal structure (top) and unfolded electronic band structure (bottom) of adsorbed Fe atoms on MoS_2 monolayer (Fe atom is colored in red, Mo in violet, and sulfur in yellow) modelled with a 3×3 supercell (highlighted in orange). The color code in the band structure is proportional to the orbital character red for $d_{xy}/d_{x^2-y^2}$ and blue for d_{z^2}. Grey lines indicate the band structure of pristine MoS_2. (b) Structural model and electronic band structure of MoS_2 with a double sulfur vacancy capped with iron. (c) Structural model and unfolded electronic band structure of MoS_2 with substitutional Fe (in the Mo site) MoS_2. (d) Model for a Fe atom adsorbed at the MoS_2 armchair nanoribbon edge and its electronic structure evaluated in the bulk of the ribbon (e) and at the ribbon edge (f). (g) Cutting lines denoting the allowed wave vectors for the MoS_2 ribbon.

that the two-dimensional Γ and K points are projected onto the same one-dimensional $k = 0$. Comparing experimental ARPES data of Figs. 1(a)–1(c), we find that the following scenarios result in a VB maximum shift from K to Γ: Fe filling a Mo or S vacancy and Fe adsorbed to the MoS_2 island edge. We rule out the Fe adsorption on top as a possibility for the observed VB maximum shift to Γ. Taking into account that substitutionally incorporated Fe is theoretically predicted to be unstable [11], we conclude that the Fe adsorbed to the edge of MoS_2 islands is mainly responsible for the observed changed of electronic and optical properties.

III. CONCLUSION AND OUTLOOK

We have shown that Fe deposited on MoS_2/graphene at low temperature is physisorbed to graphene and MoS_2. Upon annealing, the Fe is mobile and becomes stabilized by binding to the edge of MoS_2 flakes, forming a 2D core-shell structure with Fe along the edge of an MoS_2 island. Due to the large edge to bulk ratio in epitaxially grown MoS_2, even small amounts of deposited Fe can have a large effect when Fe accumulates at the MoS_2 edges. Fe adsorption changes the MoS_2 electronic structure in that it shifts the VB maximum from the K to Γ point. This change in electronic band structure is accompanied by the loss of PL. We explain the observed changes in the electronic structure and the optical properties theoretically by showing that Fe interacts differently with in-plane and out-of-plane d orbitals. The final structure, i.e., stabilized Fe clusters at the edge of epitaxial MoS_2/graphene, is not only interesting for band structure engineering but might also be useful for future experiments that probe its catalytic and magnetic properties. Finally, it might be interesting to investigate the interaction of Fe with other TMDCs such as $MoTe_2$ for which theory predicts that Fe substitution is possible [11].

IV. METHODS

A. Experimental details

We have grown MoS_2 on graphene/Ir(111) according to a previously published recipe [16]. Samples grown in that way have monolayer thickness which is evidenced by having only a single VB in ARPES [24,25], by having a PL intensity [24] and by the fact that STM shows only monolayer islands. We performed Fe doping *in situ* by evaporation of Fe (via electron bombardment) onto the cooled sample. The amount of deposited Fe was calibrated using a quartz microbalance. For the ARPES experiment (BaDElPh beamline [26] of the Elettra synchrotron in Trieste, Italy), 0.05 Å of Fe have been deposited with the sample (0.7 ML MoS_2 coverage) at $T =$ 15 K. The Fe height is given with respect to the Fe(110) bcc structure. Next, we annealed the sample to room temperature

for ∼10 min. Afterward, the sample was cooled to 15 K again and we performed ARPES. For PL, we performed sample synthesis *in situ* as described above. The PL measurements and Fe doping were performed in a home-built UHV optical setup at 4 K [24,27]. Fe doping experiments were carried out in three steps so the amount of Fe deposited after the third step was equal to 0.05 Å. For STM measurements, the MoS_2 sample synthesis (0.4 ML coverage) and Fe doping was also performed *in situ*. The Fe evaporation has been performed with the sample at $T = 30$ K. The amount of Fe deposited in the STM experiment was chosen as 0.08 Å.

B. Computational details

Calculations were performed within first-principles density functional theory using the VIENNA AB-INITIO SIMULATION PACKAGE [28,29]. We used projected augmented-wave pseudopotentials [30] and the generalized gradient approximation [31] to the exchange-correlation energy with an energy cutoff up to 350 eV (560 eV for the augmentation charges) for all calculations. We considered the unit cell of 1H-MoS_2 at the experimental lattice constant [32,33], including about 12 Å of vacuum in the out-of-plane direction. From this, we have constructed a 3×3 supercell to simulate the Fe-substituted bulk and armchair nanoribon systems, respectively. The choice of the 3×3 supercell was done considering the computational cost of the many different calculations performed, having in any case tested the convergence with respect to a larger 4×4 unit cell which confirmed that the dimension of the supercell was converged. In the nanoribbon, we included the same 12 Å of vacuum in the nonperiodic direction. The Fe atom was substituted to a Mo atom in the bulk case and added at the edges of the nanoribbon in the position that the Mo atom would occupy in the natural continuation of the crystal keeping the innermost atoms fixed in the positions of the monolayer (atoms at distance $\gtrsim$12 Å from the edge). Integration over the BZ was performed using uniform Monkhorst and Pack grids [34] depending by the system: a $24 \times 24 \times 1$ for the MoS_2 unit cell, a $8 \times 8 \times 1$ for the 3×3 supercell, and a $12 \times 1 \times 1$ grid in the nanoribbon case. For all calculations, a Gaussian smearing parameter of $\sigma = 0.02$ eV was included. The relaxation was performed until the forces dropped below 0.1 mRy/(a.u.) and the energy threshold for total energy was set to 0.1 mRy for all calculations. The unfolding processes were performed using BAND-UP software [35,36]. Core-level shifts are calculated using a 6×6 supercell in the final-state approximation, exciting one electron from the core state of a specific atom directly into the VB [37].

ACKNOWLEDGMENTS

N.E., J.F., T.K., T.M., and A.G. acknowledge funding through Deutsche Forschungsgemeinschaft (DFG, German Research Foundation) within CRC 1238 (Project No. 277146847, Subprojects No. A01 and No. B06). B.V.S. and A.G. acknowledge DFG Project No. SE2575/4-1, "Engineering the electronic band structure of transition metal dichalcogenide heterostructures in device geometries". M.B. and A.G. acknowledge the TIDE graduate school (Project No. B2). J.F. acknowledges financial support from the DFG SPP 2137 (Project FI No. 2624/1-1). We acknowledge Elettra Sincrotrone Trieste for providing access to its synchrotron radiation facilities. The ARPES experiments have been supported by the Horizon 2020 EC program under Grant Agreement No. 730872 (CALIPSOplus). A.M. and D.S. acknowledge the BMBF (Grants No. 05K19KER and No. 0519ODR, respectively). We thank the Helmholtz-Zentrum Berlin für Materialien und Energie for the allocation of synchrotron radiation beamtime. C.T. and G.P. acknowledge a CINECA award under the ISCRA initiative for access to high performance computing resources. G.P. acknowledges financial support from the Italian Ministry for Research and Education through the PRIN-2017 project "Tuning and understanding Quantum phases in 2D materials"—Quantum 2D (IT-MIUR Grant No. 2017Z8TS5B). G.P. acknowledges funding by the European Union—NextGenerationEU under the Italian Ministry of University and Research (MUR) National Innovation Ecosystem Grant No. ECS00000041–VITALITY–CUP E13C22001060006.

[1] M. Chhowalla, H. S. Shin, G. Eda, L.-J. Li, K. P. Loh, and H. Zhang, Nat. Chem. **5**, 263 (2013).
[2] D. Pasquier and O. V. Yazyev, 2D Mater. **6**, 025015 (2019).
[3] K. V. Shanavas and S. Satpathy, Phys. Rev. B **91**, 235145 (2015).
[4] K. F. Mak, C. Lee, J. Hone, J. Shan, and T. F. Heinz, Phys. Rev. Lett. **105**, 136805 (2010).
[5] K. Zollner, Paulo E. Faria Junior, and J. Fabian, Phys. Rev. B **100**, 195126 (2019).
[6] D. Voiry, A. Goswami, R. Kappera, C. de Carvalho Castro e Silva, D. Kaplan, T. Fujita, M. Chen, T. Asefa, and M. Chhowalla, Nat. Chem. **7**, 45 (2015).
[7] M. Kang, B. Kim, S. H. Ryu, S. W. Jung, J. Kim, L. Moreschini, C. Jozwiak, E. Rotenberg, A. Bostwick, and K. S. Kim, Nano Lett. **17**, 1610 (2017).
[8] Y. C. Cheng, Z. Y. Zhu, W. B. Mi, Z. B. Guo, and U. Schwingenschlögl, Phys. Rev. B **87**, 100401(R) (2013).
[9] A. N. Andriotis and M. Menon, Phys. Rev. B **90**, 125304 (2014).
[10] N. Onofrio, D. Guzman, and A. Strachan, J. Appl. Phys. **122**, 185102 (2017).
[11] J. Karthikeyan, H.-P. Komsa, M. Batzill, and A. V. Krasheninnikov, Nano Lett. **19**, 4581 (2019).
[12] Q. Li, X. Zhao, L. Deng, Z. Shi, S. Liu, Q. Wei, L. Zhang, Y. Cheng, L. Zhang, H. Lu, W. Gao, W. Huang, C.-W. Qiu, G. Xiang, S. J. Pennycook, Q. Xiong, K. P. Loh, and B. Peng, ACS Nano **14**, 4636 (2020).
[13] R. Gangwar, D. Pandey, S. Kancharlapalli, D. Raychaudhuri, A. Chakrabarti, A. Banerjee, and T. K. Ghanty, J. Phys. Chem. C **125**, 1493 (2021).
[14] Y. Wang, B. Wang, R. Huang, B. Gao, F. Kong, and Q. Zhang, Physica E **63**, 276 (2014).
[15] J. Hong, Z. Hu, M. Probert, K. Li, D. Lv, X. Yang, L. Gu, N. Mao, Q. Feng, L. Xie, J. Zhang, D. Wu, Z. Zhang, C. Jin, W.

Ji, X. Zhang, J. Yuan, and Z. Zhang, Nat. Commun. **6**, 6293 (2015).
[16] J. Hall, B. Pielić, C. Murray, W. Jolie, T. Wekking, C. Busse, M. Kralj, and T. Michely, 2D Mater. **5**, 025005 (2018).
[17] A. N. Koveshnikov, R. H. Madjoe, J. Karunamuni, R. L. Stockbauer, and R. L. Kurtz, J. Appl. Phys. **87**, 5929 (2000).
[18] G.-B. Liu, W.-Y. Shan, Y. Yao, W. Yao, and D. Xiao, Phys. Rev. B **88**, 085433 (2013).
[19] E. Khestanova, T. Ivanova, R. Gillen, A. D'Elia, O. N. Gallego Lacey, L. Wysocki, A. Grüneis, V. Kravtsov, W. Strupinski, J. i. Maultzsch, V. Kandyba, M. Cattelan, A. Barinov, J. Avila, P. Dudin, and B. V. Senkovskiy, ACS Photonics **10**, 1159 (2023).
[20] M. M. Ugeda, A. J. Bradley, S.-F. Shi, F. H. da Jornada, Y. Zhang, D. Y. Qiu, W. Ruan, S.-K. Mo, Z. Hussain, Z.-X. Shen, F. Wang, S. G. Louie, and M. F. Crommie, Nat. Mater. **13**, 1091 (2014).
[21] S. Trishin, C. Lotze, N. Bogdanoff, F. von Oppen, and K. J. Franke, Phys. Rev. Lett. **127**, 236801 (2021).
[22] S. Helveg, J. V. Lauritsen, E. Lægsgaard, I. Stensgaard, J. K. Nørskov, B. S. Clausen, H. Topsøe, and F. Besenbacher, Phys. Rev. Lett. **84**, 951 (2000).
[23] A. Bruix, H. G. Füchtbauer, A. K. Tuxen, A. S. Walton, M. Andersen, S. Porsgaard, F. Besenbacher, B. Hammer, and J. V. Lauritsen, ACS Nano **9**, 9322 (2015).
[24] N. Ehlen, J. Hall, B. V. Senkovskiy, M. Hell, J. Li, A. Herman, D. Smirnov, A. Fedorov, V. Yu Voroshnin, G. Di Santo, L. Petaccia, T. Michely, and A. Grüneis, 2D Mater. **6**, 011006 (2018).
[25] V. Voroshnin, A. V. Tarasov, K. A. Bokai, A. Chikina, B. V. Senkovskiy, N. Ehlen, D. Y. Usachov, A. Grüneis, M. Krivenkov, J. Sánchez-Barriga, and A. Fedorov, ACS Nano **16**, 7448 (2022).
[26] L. Petaccia, P. Vilmercati, S. Gorovikov, M. Barnaba, A. Bianco, D. Cocco, C. Masciovecchio, and A. Goldoni, Nucl. Instrum. Methods Phys. Res., Sect. A **606**, 780 (2009).
[27] M. Hell, N. Ehlen, B. V. Senkovskiy, E. H. Hasdeo, A. Fedorov, D. Dombrowski, C. Busse, T. Michely, G. di Santo, L. Petaccia, R. Saito, and A. Grüneis, Nano Lett. **18**, 6045 (2018).
[28] G. Kresse and J. Furthmüller, Phys. Rev. B **54**, 11169 (1996).
[29] G. Kresse and J. Furthmüller, Comput. Mater. Sci. **6**, 15 (1996).
[30] P. E. Blöchl, Phys. Rev. B **50**, 17953 (1994).
[31] J. P. Perdew, K. Burke, and M. Ernzerhof, Phys. Rev. Lett. **77**, 3865 (1996).
[32] M. Li, J. Shi, L. Liu, P. Yu, N. Xi, and Y. Wang, Sci. Technol. Adv. Mater. **17**, 189 (2016).
[33] G. Anemone, A. A. Taleb, A. Castellanos-Gomez, and D. Farías, 2D Mater. **5**, 035015 (2018).
[34] H. J. Monkhorst and J. D. Pack, Phys. Rev. B **13**, 5188 (1976).
[35] P. V. C. Medeiros, S. Stafström, and J. Björk, Phys. Rev. B **89**, 041407(R) (2014).
[36] P. V. C. Medeiros, S. S. Tsirkin, S. Stafström, and J. Björk, Phys. Rev. B **91**, 041116(R) (2015).
[37] L. Köhler and G. Kresse, Phys. Rev. B **70**, 165405 (2004).